Supporting Information for "Anisotropic Tomography around La Réunion Island from Rayleigh Waves"

A. Mazzullo,[1] Eléonore Stutzmann,[1] Jean-Paul Montagner,[1] S. Kiselev,[4] S. Maurya,[5] G. Barruol,[1,2] and K. Sigloch[3]

———

Corresponding author: A. Mazzullo Institut de Physique du Globe de Paris, Sorbonne Paris Cité, CNRS UMR 7154, 4 Place Jussieu, 75005 Paris France (alessandro@ipgp.fr)

[1]Département de Simologiem Institut de

Physique du Globe,4,Place Jussieu,75252

Paris cedex 05, France.

[2]Laboratoire Geosciences, Universite de

La Réunion, Saint-Denis Réunion, France.

[3]Department of Earth Sciences,

University of Oxford, UK.

[4]Institute of Physics of the Earth,

Bolshaya Gruzinskaya str., 10-1 Moscow

123242, Russia.

[5]Berkeley Seismological Laboratory,

University of California, Berkeley, CA

94720, USA

Contents of this file

Additional Supporting Information (Files uploaded separately)

None

Introduction

Text S1 presents the synthetic tests on the regionalization and the phase/ group velocity inversion to retrieve the S-wave velocity model. Figures S1 to S6 accompany Text S1.

Text S2 and Figures S7 to S10 describe how the crustal model is taken into account.

Text S3 and Figures S11 to S19 present the comparison between the present model and the three published models for isotropic S-wave velocities and anisotropy fast directions.

Text S1. Synthetic tests

S1.1 Tests on the regionalized phase/ group velocity lateral reliability

The parameters of the *Regionalization* method were extensively tested to find the best combination of σ_m and L_{corr}, which corresponds to the balance between the variance reduction and χ^2. The lateral resolution is estimated with synthetic tests of the phase/ group velocity and azimuthal anisotropy. The path density and the azimuthal coverage in the tests correspond to the real path coverage. These synthetic tests are presented in Figures (S1-S2) for the phase velocities, and Figures (S3-S4) for the group velocities. The synthetic model is a checkerboard with positive/ negative velocity anomalies and different

———————

anisotropic azimuthal directions. We consider 500-km-wide square velocity spots with an increment of $\pm 2\%$ on the velocity with respect to the reference model, and anisotropy anomalies of 2%. The inversion is performed using the same parameters as for the real data (*a-priori* error, correlation length). The results presented in Figures (S1-S3) show that the synthetic velocity anomalies are correctly recovered both in location and amplitude for periods of 36, 100, and 200 s, even though the anomalies are smoothed by the correlation length of 200 km. For the same periods, Figures (S2-S4) show that the anisotropic anomalies are recovered in direction and amplitude for the phase and group velocities, especially in the center area where the azimuthal path coverage is more uniform. Therefore, the azimuthal anisotropy results should not be interpreted at the edges of the area.

S1.2 Synthetic tests on the local inversion for retrieving the S-wave velocity model

The inversion of the phase and group velocities is performed locally at each longitude/ latitude of the grid. Hereafter, we demonstrate with synthetic tests that the number of splines and the S-wave velocity model can be accurately recovered by the inversion. We construct the synthetic model as follows. We take a decimal number of splines at random, say 3.9. The integer part, *i.e.*, 3, refers to the number of splines. The fractional part shows how tight the spline basis is compressed to the Earth surface. As the fractional part is almost 1 here (*i.e.*, 0.9), the spline basis is strongly compressed toward the surface, and it is about to get a 4th spline at the bottom. Examples of the spline basis are plotted in Figure S5 (bottom) for spline numbers of 3.1, 3.9, and 4.1. We select at random the amplitudes of the three splines, and we construct the synthetic Vs model using Equation

(5). Figure S5 shows the three synthetic models and the corresponding synthetic group velocities (in red) for the spline basis numbers of 3.1, 3.9, and 4.1. These group velocities are the input data for the one-dimensional depth inversion, and the *a-priori* data error is set to 0.5%. In the inversion procedure, the number of splines and their amplitudes are unknown. The total depth of the model (*i.e.*, 300 km) and the crust model are known. The inversion results are plotted in blue and the extreme range of the model parameters explored are plotted in green. We use M = 3.1, 3.9, and 4.1 for the three synthetic spline basis and we recover M = 3.00203, 3.66636, and 4.00332, which are the correct numbers of the splines, with slightly different shapes. The inverted S-wave model and the corresponding group velocity are correctly recovered within the error bars.

We then performed a second set of synthetic tests to investigate the resolution at depth of the inverted model. Three input models were created, with one smooth anomaly placed at different depths. Figure (S6) shows the synthetic and inverted S-wave velocity models. Although the amplitude is difficult to retrieve, it is possible to appreciate that the anomaly is recovered in all cases at the right depth. The vertical smoothing effect that increases with depth is partly due to the smoothing parameters of the inversion, and mainly to the lower sensitivity of the surface waves at depth.

Text S2. Crustal model analysis

The period range of the phase and group velocities used in this study (16 s to 240 s) does not allow the crustal structure to be efficiently constrained. However, the surface waves are very sensitive to variations in the first layers of the Earth. An incorrect crustal model can affect the results of the inversion and the final velocity model. For this reason, it is essential to take into account the lateral variations of the crustal structure, with the

incorporation of all *a-priori* knowledge on the composition of the crust, in order to use the best possible crustal model. Crust1.0 is the starting point of our analysis on the crust in the western Indian Ocean. This model is defined on a 1-degree grid and is based on a database of crustal models from seismically active sources and receiver functions, and in the areas where such constraints are still missing, gravity studies. In the depth inversions here, Crust1.0 was locally modified to avoid strong lateral variations that might bias the V_{sv} model. The smooth a priori model is constructed as follows.

In each point of a 1-degree longitudinal-latitudinal grid, phase and group velocities are computed in the period band from 16 s to 200 s for the model composed of the local Crust1.0 and PREM where the 220 km discontinuity is smoothed. The resulting phase and group velocity maps are smoothed with a correlation length of 800 km, which is approximately equal to the longest wavelength theoretically observed with the present velocity calculated at a period of 240 s ($\lambda_{max} = 240s * 3.6km/s = 860km$). At each grid point, the initial and smoothed group and phase velocities are compared.

For 30% of the grid points in the map, the original and smoothed phase/ group velocities are almost identical. Thus, the crustal smoothing with an 800 km length will have no influence on the inversion for the mantle velocities, and at these grid points, the original Crust1.0 plus smoothed PREM is used as the starting model for the mantle velocity inversion (see example in Fig. S7).

For the remaining grid points, the smoothed group and phase velocities are inverted in the same period range as for the mantle inversion (*i.e.*, 16 s to 200 s) to obtain the smoothed crustal model. At each grid point, this crustal inversion uses for the starting model a combination of local crust1.0 plus smoothed PREM. Because the period range

of 16 s to 200 s does not enable to retrieve simultaeously the layer thicknesses and velocities in the crust, we keep the original local crust1.0 values for V_{sv}, V_p, and ρ, and only inverted for the layer thicknesses. In the procedure, only three parameters are explored, to minimize the misfit function: ocean thickness, sediment thickness, and total thickness of the remaining crust. Once the 3 layer thicknesses are retrieved, all other crustal layer thicknesses are varied proportionally. After inversion, the ocean thickness is different from the starting value only close to the ocean-continent boundaries. In continents, the ocean layer has zero thickness.

For 50% of the grid points (see example in Fig. S8), the inverted crustal model is well resolved (it explains the smoothed phase and group velocities) and it can be used as a priori model for the mantle structure inversion.

It was found that for the 20% of the grid points, which are mainly located in the continental area, the inverted crustal model is not well resolved and there is a large discrepancy between the phase and group velocities computed for this model and the smoothed phase and group velocities (Fig. S9). For these points, a direct V_s averaging is used: the upper 80 km of the model crust 1.0 plus PREM is subdivided into 68 layers of 0.25-km thickness. Each layer is meaned laterally with a Hamming window of 800-km width.

Finally we end up with a V_s crustal model on a grid of 1 deg x 1 deg that is a smoothed version of crust1.0 plus PREM (without the 220 km discontinuity). It consists of three types of treatments:

- Original nonsmoothed crust1.0 for 30% of the grid points;

- Crust1.0 corrected by inversion for the layer thicknesses for 50% of the grid points;

- Directly smoothed V_p, V_s ρ for 20% of the grid points.

Figure S10 shows the Moho depth for the original Crust1.0. This smoothed model is used as the starting model for the inversion of phase and group velocities regionalized with a correlation of 800 km.

Text S3. Comparisons with global models

We compared the present model with three published global models: 3D2015 [*Debayle et al.*, 2016]; BM12UM [*Burgos et al.*, 2014]; and SL2013sv [*Schaeffer and Lebedev*, 2013].

- The **3D2015** model [*Debayle et al.*, 2016] is based on the automated waveform modeling of 1,359,470 Rayleigh wave fundamental modes and five first overtone records, up to the maximum period range of 50 s to 350 s. The synthetics are computed in a one-dimensional model that is adapted to each ray, which includes a path-specific crust structure. The tomographic inversion is performed in two steps, similar to the present study. The regionalization [*Debayle and Sambridge*, 2004] is performed with a horizontal correlation of length $L = 200km$ for both the isotropic and anisotropic parameters in the upper mantle. In the second step, the local dispersion curves are inverted to obtain the shear velocity and azimuthal anisotropy. As the dataset contains fundamental modes and overtones, it can resolve deeper structures than the present model.

- The **BM12UM** model [*Burgos et al.*, 2014] is derived from compiled Rayleigh and Love wave group and phase velocities. The dataset contains more than 300,000 independent surface-wave dispersion measurements, with a maximum period range of 16 s to 315 s. The tomographic inversion is also performed in two steps, similar to the present study. The regionalization [*Debayle and Sambridge*, 2004] is performed with a correlation length of $L_i = 400km$ for the isotropic part and $L_i = 800km$ for the anisotropic part. Then, the

local crustal model is inverted using a Monte Carlo approach with the CRUST 2.0 starting model [*Bassin et al.* , 2000]. Finally, local inversion is performed using the first-order perturbation theory for the transverse isotropic medium with vertical symmetry axis, to obtain the local anisotropic S-wave velocity model.

- The **SL2013sv** model [*Schaeffer and Lebedev*, 2013] is obtained from automated multimode waveform inversion of the surface and S-wave waveforms. The method is based on the partitioned waveform inversion method [*Nolet*, 1990], although a three-dimensional reference model is used. In the first step, the data are inverted to obtain the path-average P-wave and S-wave velocity model as a function of depth. In the second step, these path-average models are inverted to obtain the anisotropic tomographic model. The complete dataset consist of $\sim$3/4 of a million broad-band seismograms. As for model 3D2015, the use of higher modes enables the resolution of deeper structures than for the present model.

S3.1 Comparison of the isotropic component of the S-wave velocity with global tomographic models

To compare the models, we first measure the correlation r between the isotropic component of the S-wave velocity in the present model and the three published models, as a function of depth, using the expression:

$$r = \frac{\sum_l (m_l - \overline{m})(M_l - \overline{M}) * \sin^2 \theta}{\sqrt{\sum_l (m_l - \overline{m})^2 * \sin^2 \theta}\sqrt{\sum_l (M_l - \overline{M})^2 * \sin^2 \theta}} \tag{1}$$

where, l is the geographical location, m and M are the shear-wave velocities of the two models considered, and θ is the colatitude. $\overline{m}$ and $\overline{M}$ are the respective mean velocities in the area studied. Figure S11 shows good correlations of between 0.65 and 0.80 for all three global models in the depth range of 50 km to 150 km. The highest correlation is

obtained with model 3D2015. The decreasing correlation at shallow depth (< 50 km) shows that the crustal models are different. Below 200 km in depth, the present model loses resolution, which would explain the decrease in the correlation at greater depth.

We also compared the models at different depths. Figures S12 - S15 show maps of the isotropic parts of the S-wave velocities for the present model RHUM17 and the three global models. At 50 km in depth, all of the models show fast anomalies related to the African continent and the oceanic lithosphere far from the ridge with comparable amplitude. All of the models also show the mid-oceanic ridge slow velocity signature. In the regions of Afar and the East African rift, the slow velocity anomalies are more intense and elongated toward the South in the 3D2015 and SL2013 models, with respect to the RHUM17 and BM12UM models. The present model clearly shows the negative anomaly between Rodrigues Ridge and the La Réunion plume (Fig. S12, black circle) that is not resolved by the global models.

At 100 km in depth, the present model shows distinct small-scale slow velocity anomalies beneath the Mascarene Basin and the Seychelles Arc (Fig. S13, black circle), whereas the global models show a smooth slow anomaly in that area.

At 150 km in depth, the present model shows a large slow velocity anomaly beneath the whole of the Mascarene Basin from the North of Seychelles down to La Réunion island in the South (Fig. S14, black circle). The global models, instead, detect an intense slow velocity signature only along the area between the CIR and the Seychelles Arc.

At 200 km in depth, the present model and model BM12UM show smooth anomalies in both the oceanic and continental areas that are consistent with the decrease in the sensitivity of the fundamental mode surface waves at depth (Fig. S15). In the present

model, the slowest velocities are beneath the northern part of the Mascarene Basin (Fig. S15, circles **A**). This slowest velocity is shifted either eastward or northward in the three global models. The Rodrigues Triple Junction (Fig. S15, circles **B**) is associated with a positive anomaly in all of the models. Finally, all of the models show a slow velocity anomaly beneath Afar and along the East African rift. This slow anomaly continues in the ocean beneath the Comores area in the present model (Fig. S15, circle **C**), although this connection with the Comores area is less clear, or is not seen, in global models.

Finally, Figure S16 shows a cross section at latitude 20^oS that goes beneath Magagascar, La Réunion, Rodrigues Ridge and the CIR. The at 150 km in depth beneath La Réunion is observed in all of the models, although the channeling toward the CIR is very clear in the present model and less clear, or not visible, in the global models. All four of these models are very different beneath Madagascar.

Text S3.2 Comparison of azimuthal anisotropy with global models

We compared the azimuthal anisotropy pattern between the present model and the three global models at 50 km and 150 km in depth. We computed the histograms of differences $\Delta\psi$ between the fast anisotropy directions in the present model and in the three global models. Figure S17 shows that the fast directions of the present model are consistent with those of models 3D2015 and BM12UM, as 60% (resp. 55%) of the direction differences are $\leq 30^o$ at both depths. For model SL2013, the proportion of the direction differences $\leq 30^o$ decreases to 45% to 50%.

We also visually compared the maps of the anisotropy fast directions for both the present model and the three global models (Fig. S19) at 50 km and 150 km in depth. For comparison, Figure S18 shows the absolute plate motion vectors for the HS3-Nuvel1A model

and the GSRM model. Between these two models, the vectors are often perpendicular. In the African plate, all four of these models consistently show that the fast directions are mainly North-South at 50 km in depth, which become East-West at 150 km in depth, which might be consistent with both the HS3-Nuvel1A model and the GSRM models.
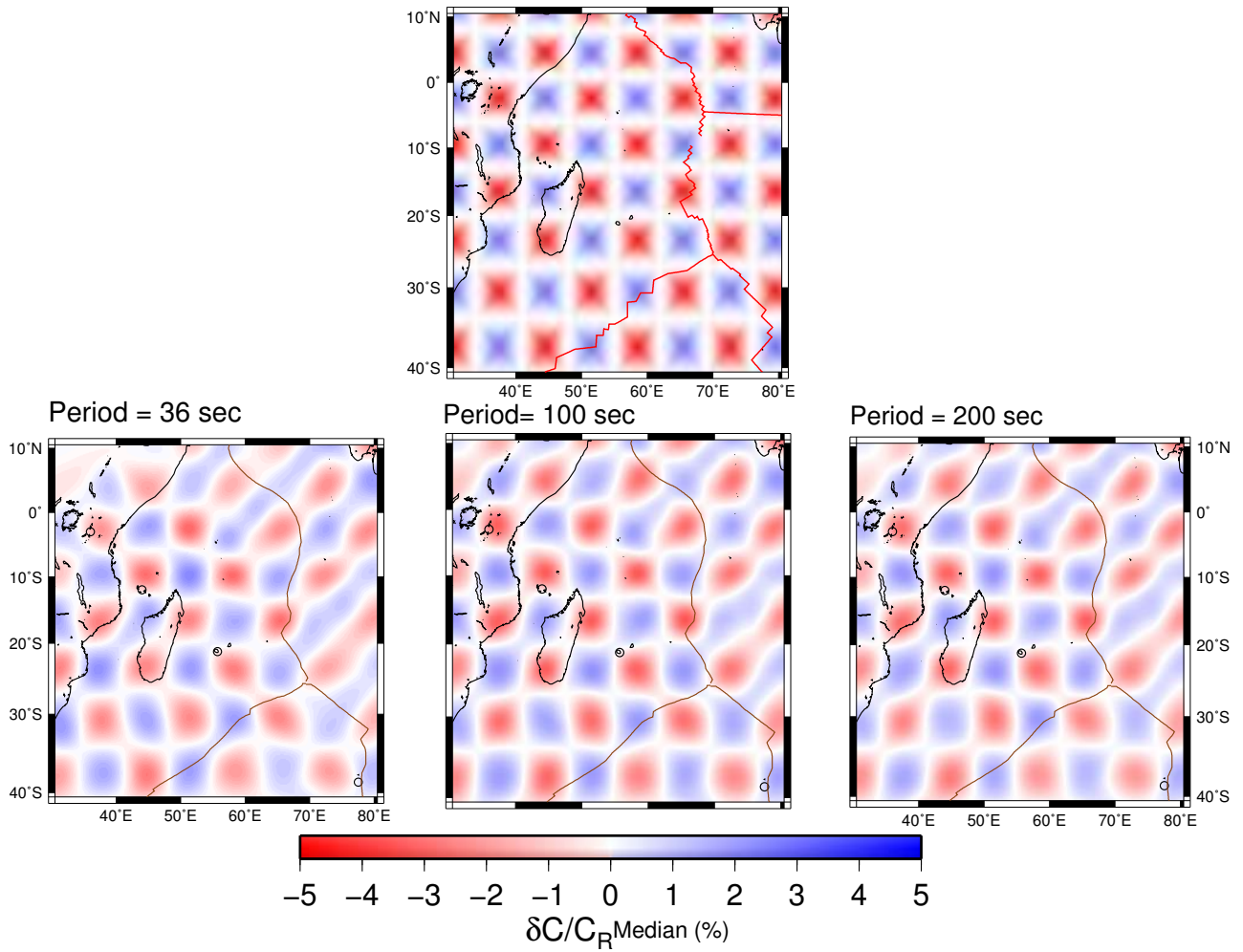
Figure S1. Checkerboard test of phase velocity, showing the reliability of the ray coverage of the area. Top: The input model. Bottom: The *Regionalization* map results for the 50, 100, 200 s periods.
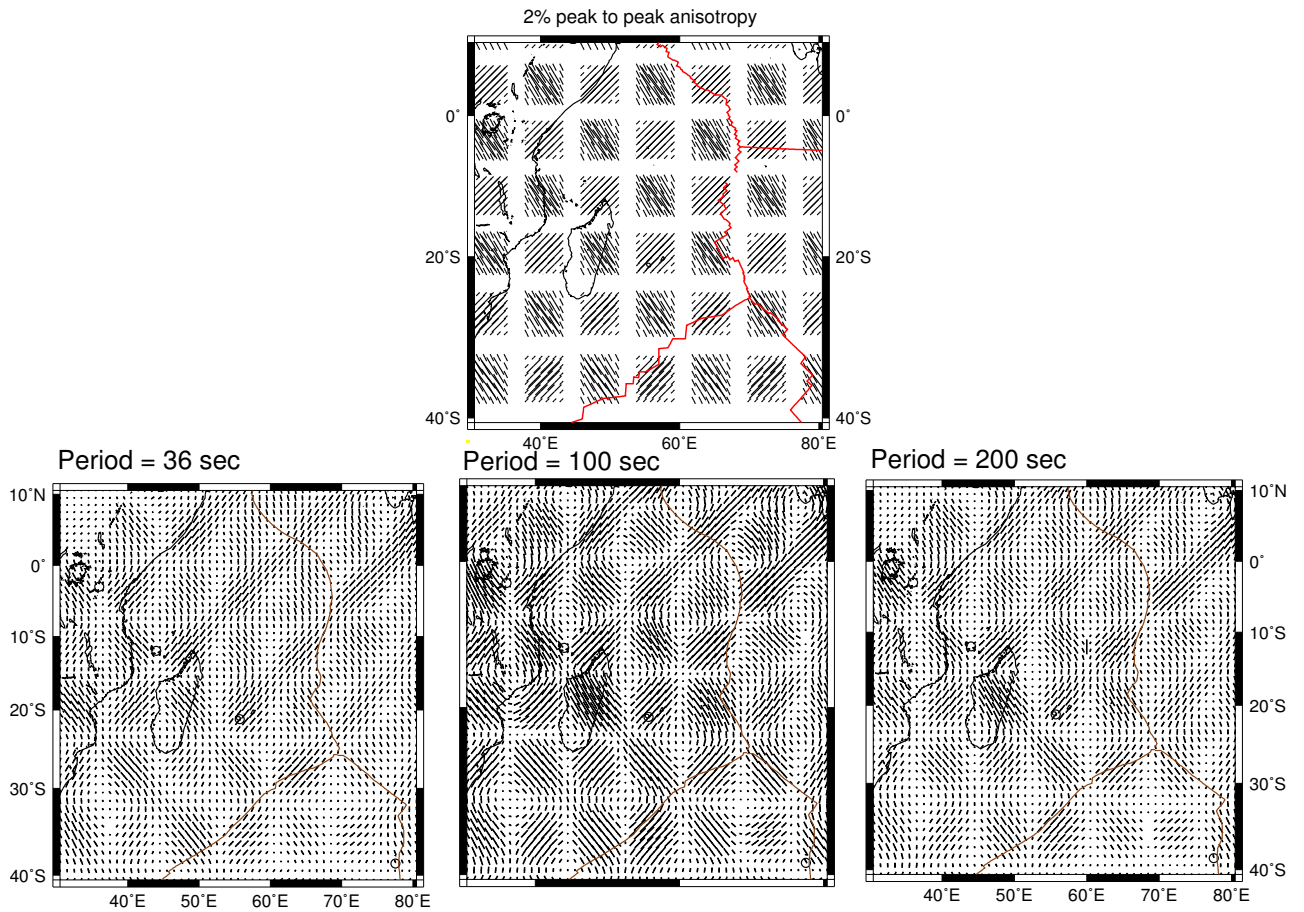
Figure S2. Checkerboard test of azimuthal anisotropy from the phase velocity measurements, showing the reliability of the ray coverage of the area. Top: The input model. Bottom: The *Regionalization* map results for the 36, 100, 200 s periods.
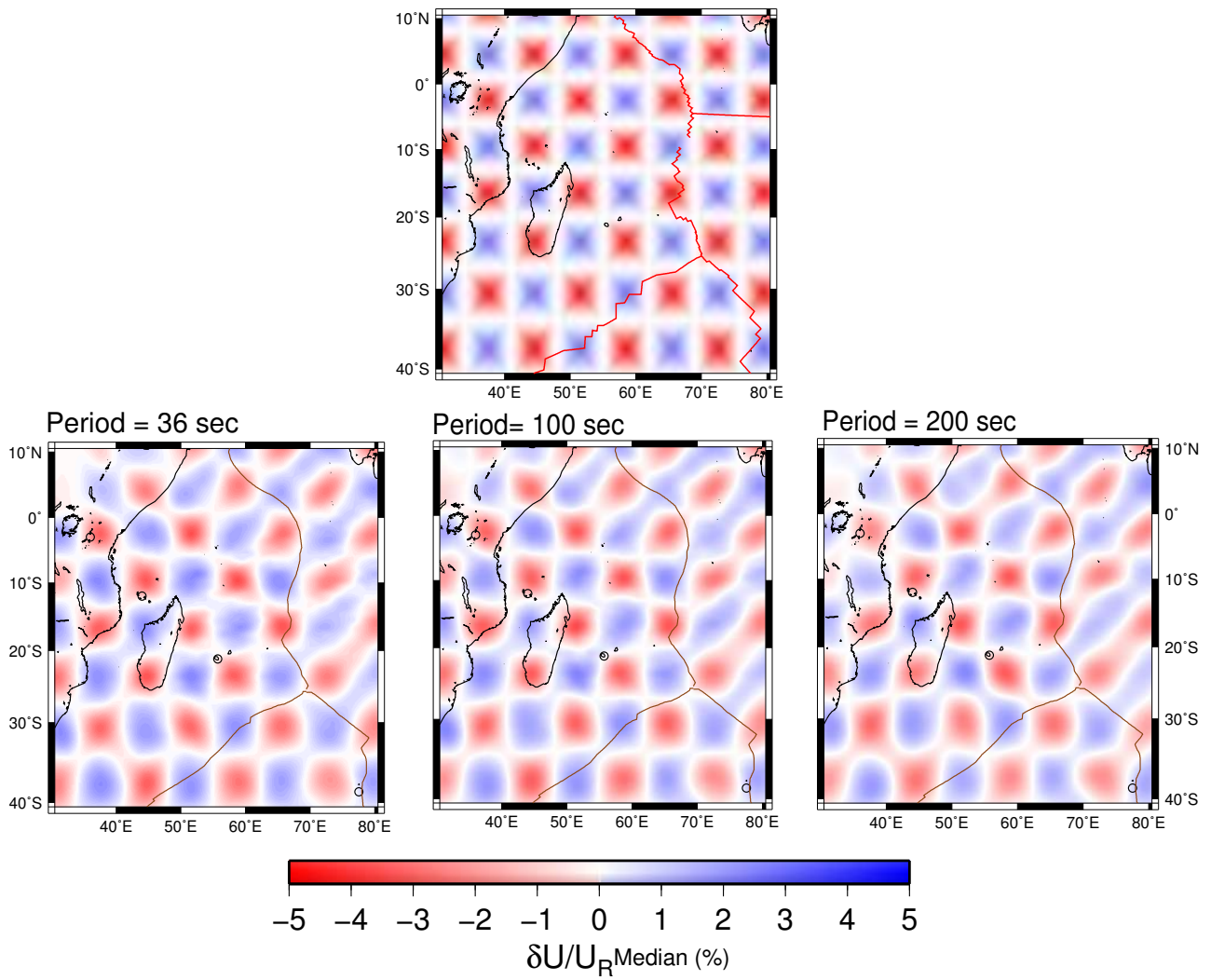
Figure S3. Checkerboard test of group velocity, showing the reliability of the ray coverage of the area. Top: The input model. Bottom: The *Regionalization* map results for the 50, 100, 200 s periods.
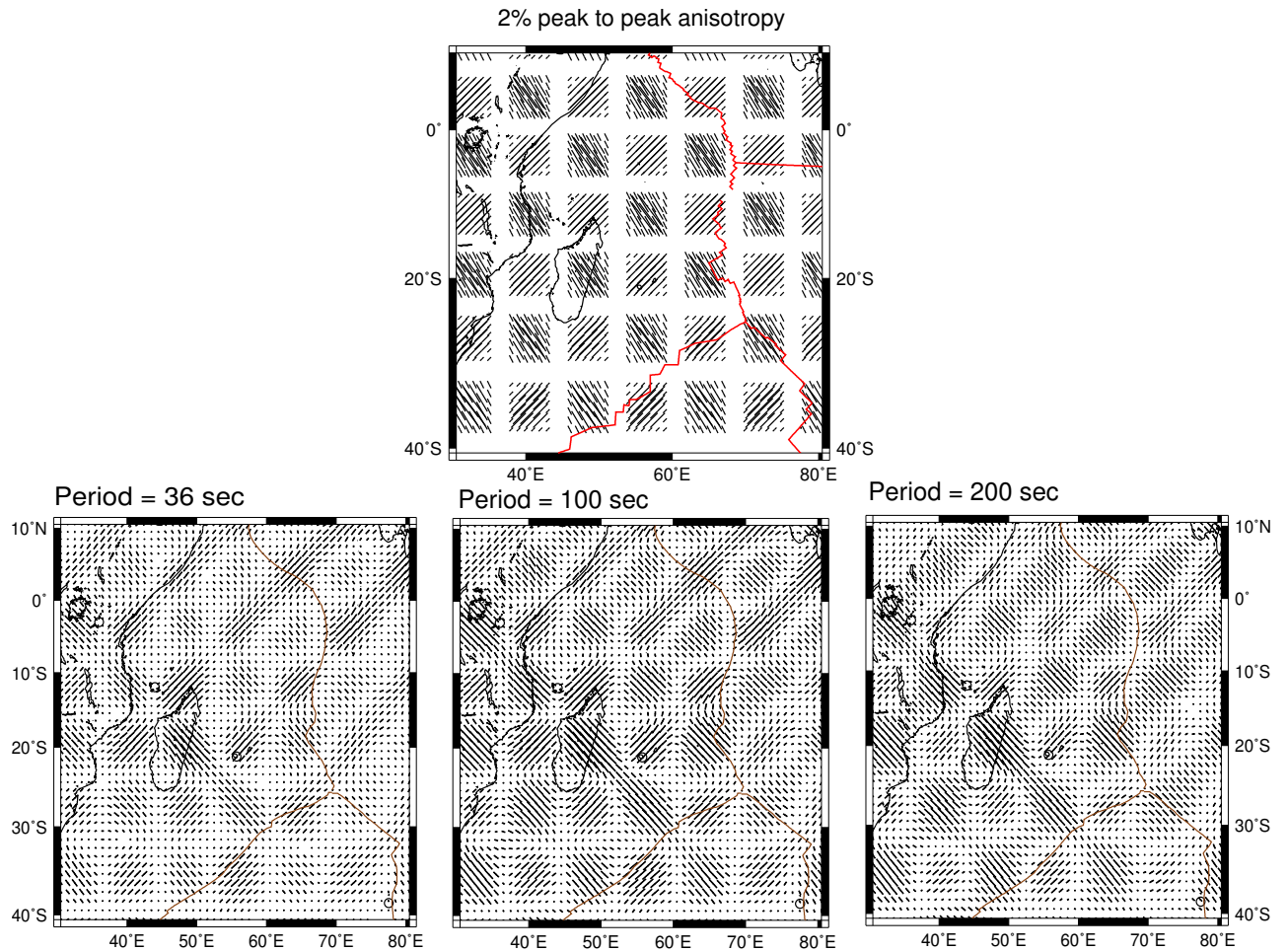
Figure S4. Checkerboard test of azimuthal anisotropy from the group velocity measurements, showing the reliability of the ray coverage of the area. Top: The input model. Bottom: The *Regionalization* map results for the 36, 100, 200 s periods.
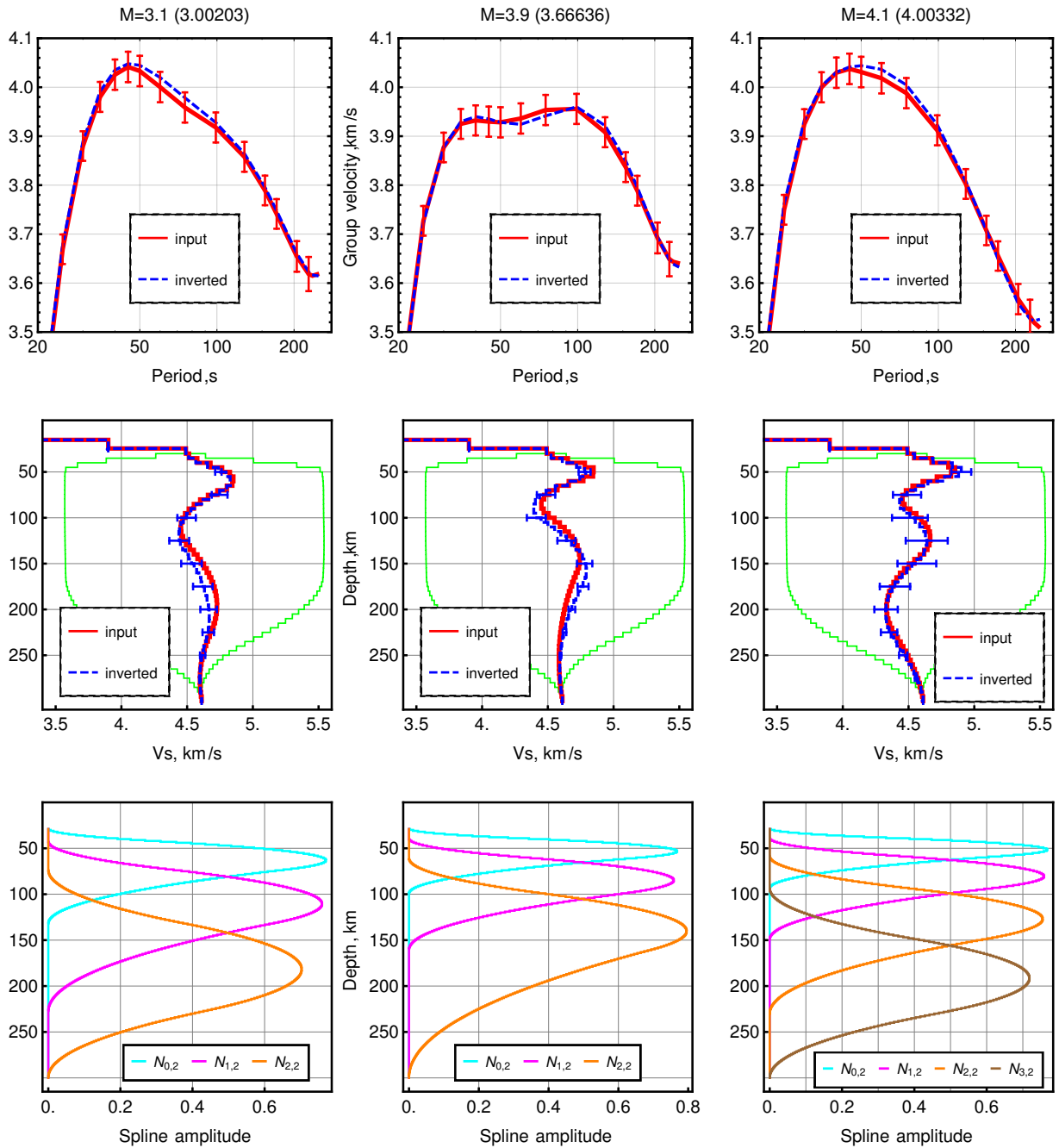
Figure S5.   Three synthetic tests to illustrate that the numbers and shapes of the splines are recovered by the inversion. The input Sv-wave velocity model (middle) and the corresponding synthetic group velocity (top) with superimposed noise are shown in red. The inverted Sv-wave velocity model (middle) and the corresponding group velocity (top) are in blue. The extreme range of the model parameter that is explored is shown by the green lines (middle). The corresponding B-spline basis functions are shown below, in different colours (bottom).

Reunion lat : −22.5 lon: 55.5
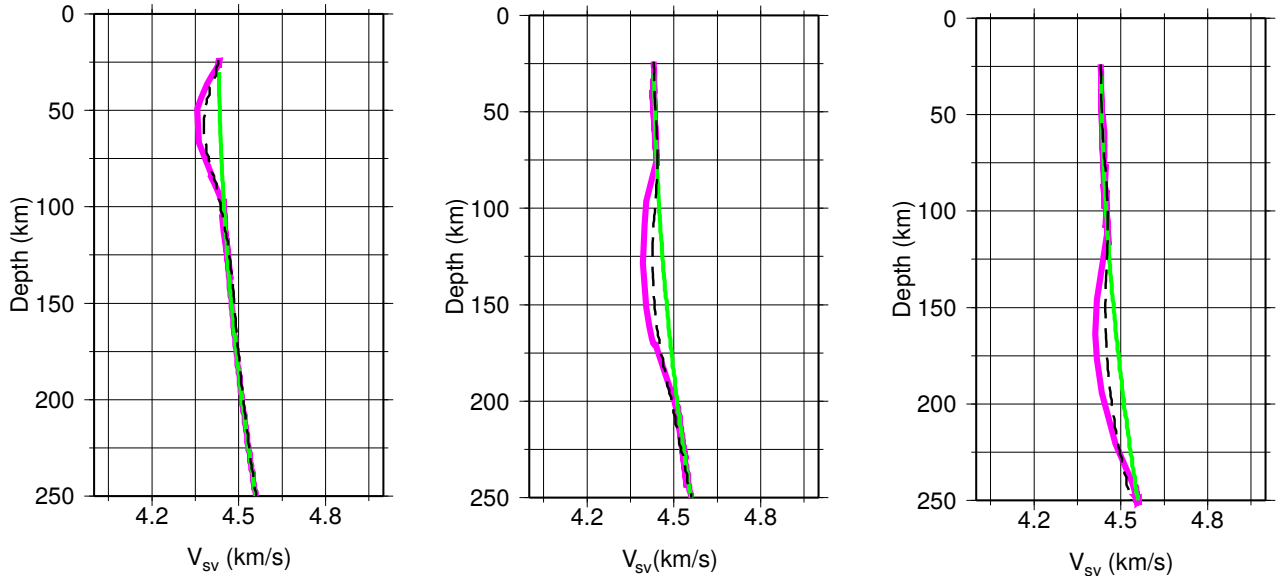
Figure S6. The synthetic (magenta) and inverted (black-dots) S-wave velocity models. The smooth anomaly is placed at different depths, and it is always well recovered.
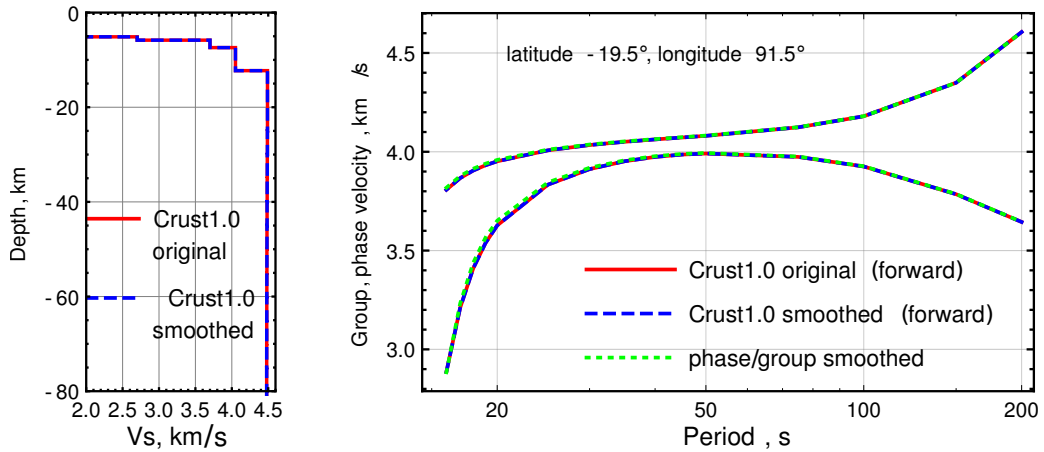
Figure S7. Crustal analysis for grid point lat. −19.5, lon. 91.5. Left: The one-dimensional V_s models for the inversion of the original Crust1.0 and the smoothed version are identical. Right: The phase and group velocity results for the original (red line) and the smoothed versions of Crust 1.0. are equal, and the original Crust 1.0 model is used for the inversion at this location.
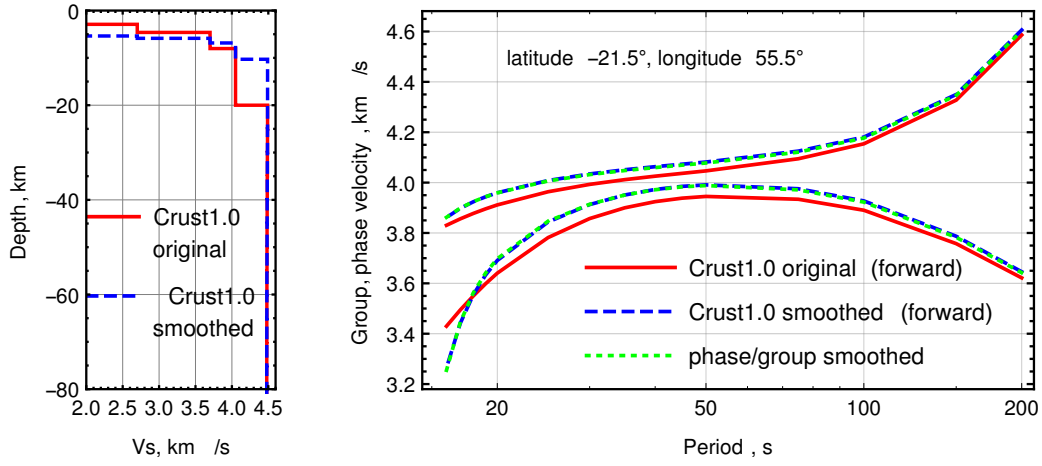
Figure S8.   Crustal analysis for the grid point lat. -21.5, lon. 55.5. Left: The one-dimensional V_s models for the inversion of the original Crust1.0, and the smoothed version. The V_s values are not inverted due to the period range of the inversion (16 s to 240 s) that only allows evaluation of the thicknesses of the layers. Right: The phase and group velocity results for the original (red line) and the smoothed version of Crust 1.0.
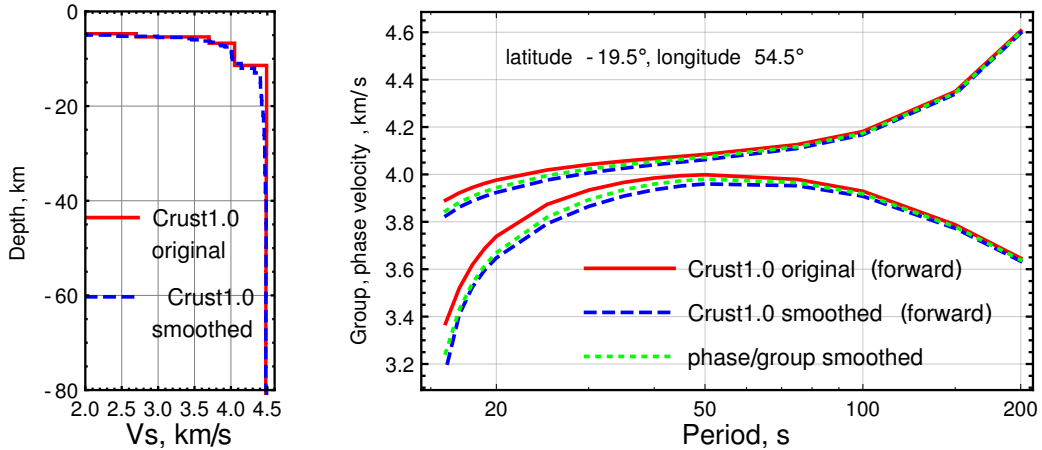
Figure S9.   Crustal analysis for grid point lat. -19.5, lon. 54.5. Left: The one-dimensional V_s models for the original Crust1.0 and the inverted smoothed version obtained by lateral averaging with a Hamming window of 800 km in width, of V_p, V_s, and ρ. Right: The phase and group velocity results for the original (red line) and the smoothed version of Crust 1.0.
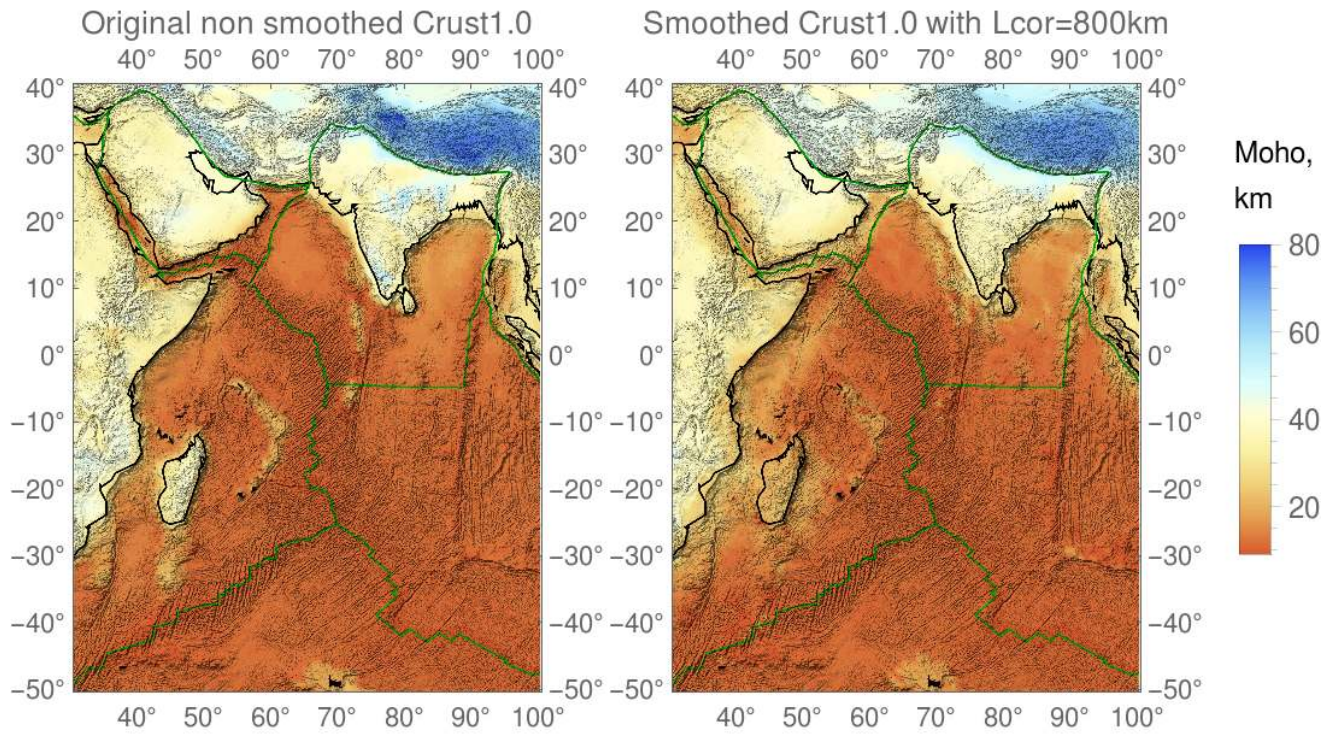
Figure S10. Left: The Moho depth for the original Crust1.0 model. Right: The resulting modified Moho depth after the crustal procedure.
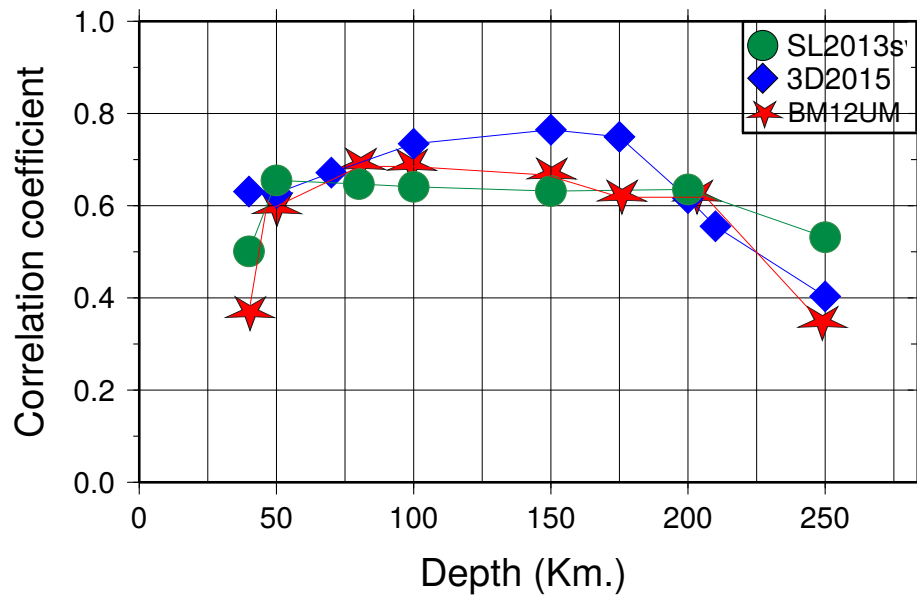
Figure S11.   Correlation coefficient between the present model RHUM17 and the three global

models SL2013s, 3D2015, and BM12UM
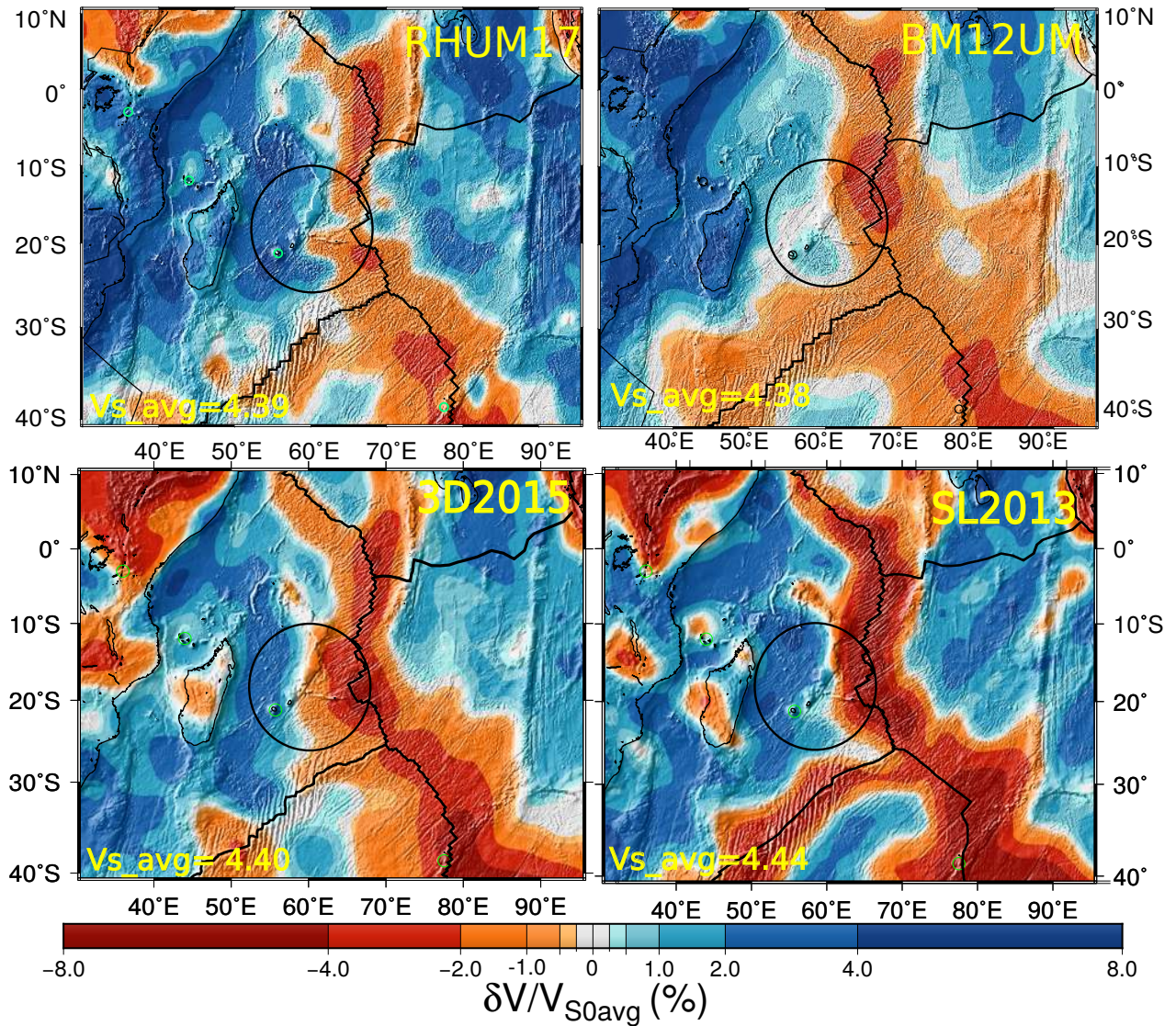
Figure S12. Comparison of shear velocity perturbation between the present model RHUM17 and the three recent global models, BM12UM, SL2013sv, and 3D2015 at 50 km in depth. Black circles indicate the area where model RHUM17 shows the shallow signature of a 'pipe-flow' connecting the La Réunion hotspot with the CIR, which is not resolved by the global models.
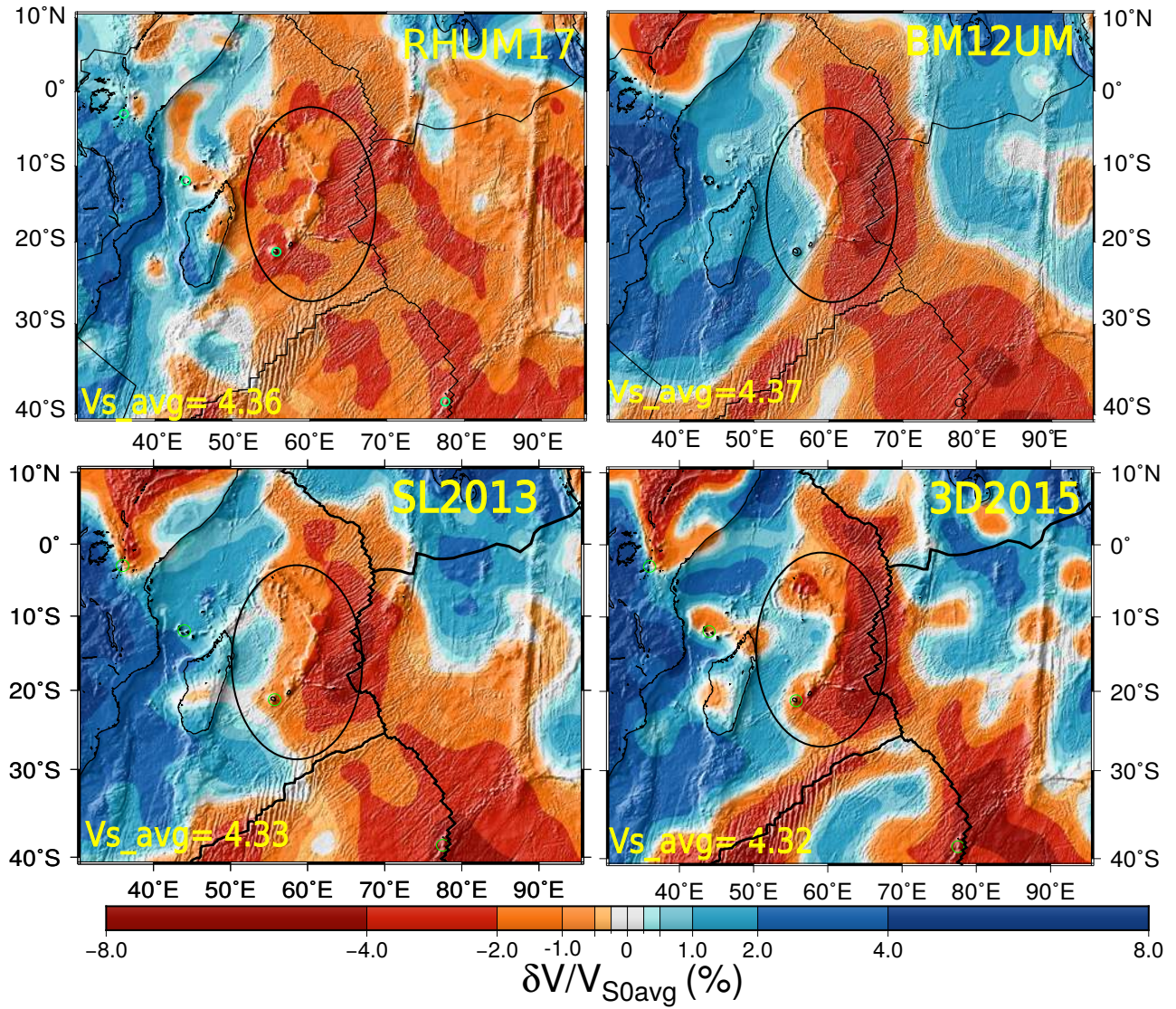
Figure S13.   Same as Figure S12, at 100 km in depth. The present model shows high lateral

resolution, andd resolves the different slow velocity anomalies beneath the Mascarene Basin.
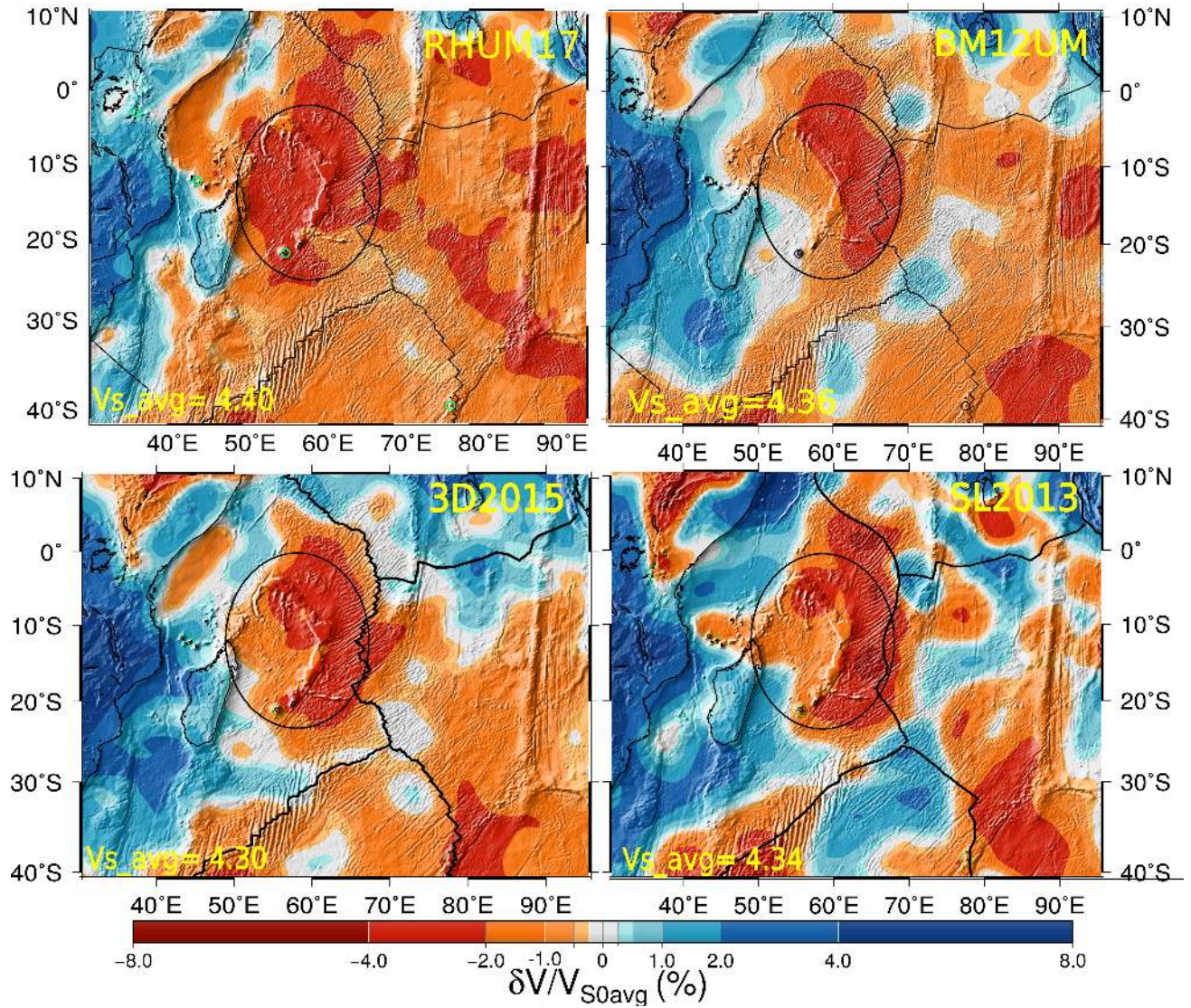
Figure S14. Same as Figure S12, at 150 km in depth. The present model shows the large slow velocity anomaly centered beneath the Mascarene Basin, while the global models place the anomaly more to the East
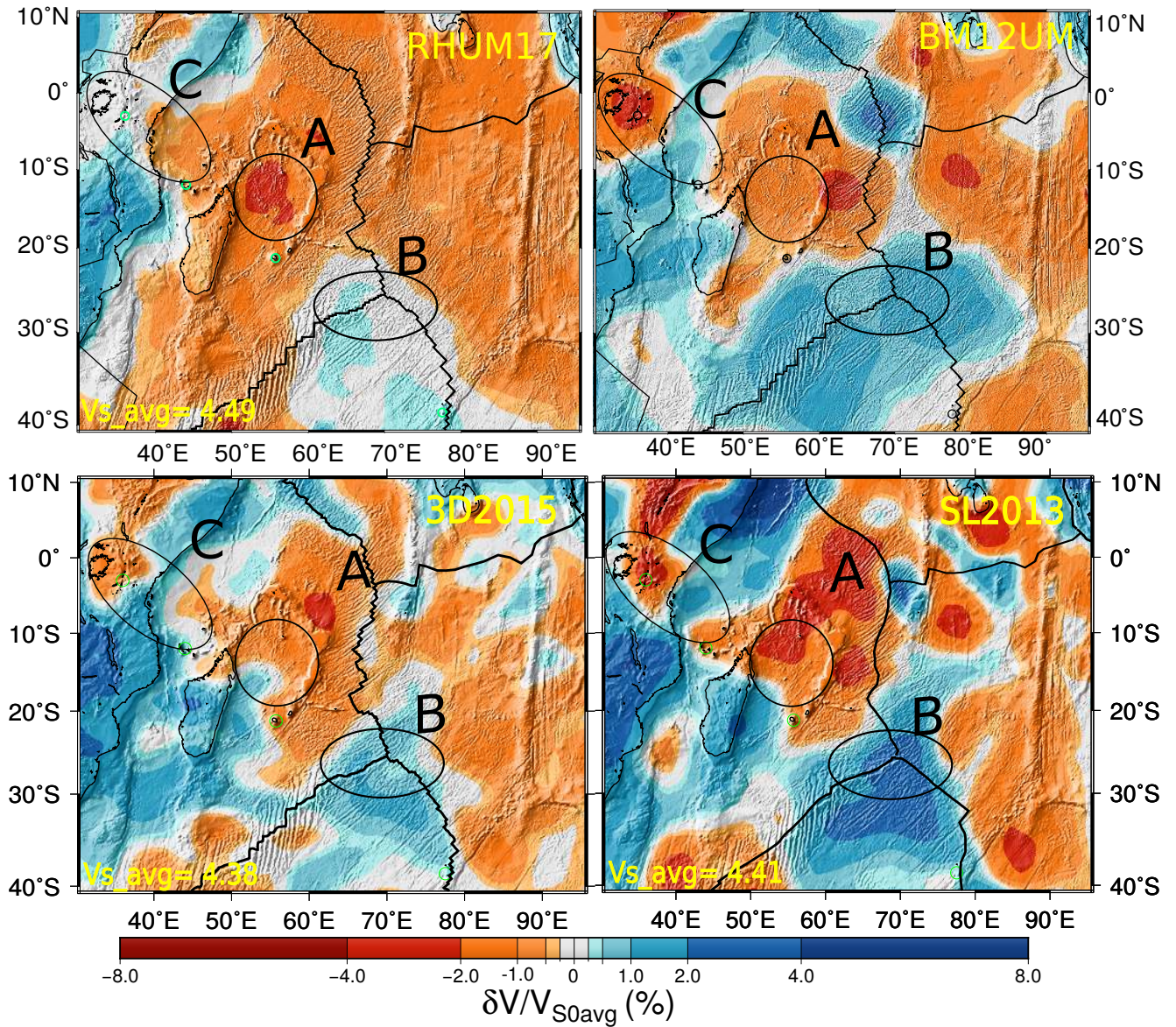
Figure S15.   Same as Figure S12, at 200 km in depth. An isolate slow velocity anomaly is see in the present model benath the North part of Mascarene Basin, while instead the other models show a more complex slow velocity anomaly setting.
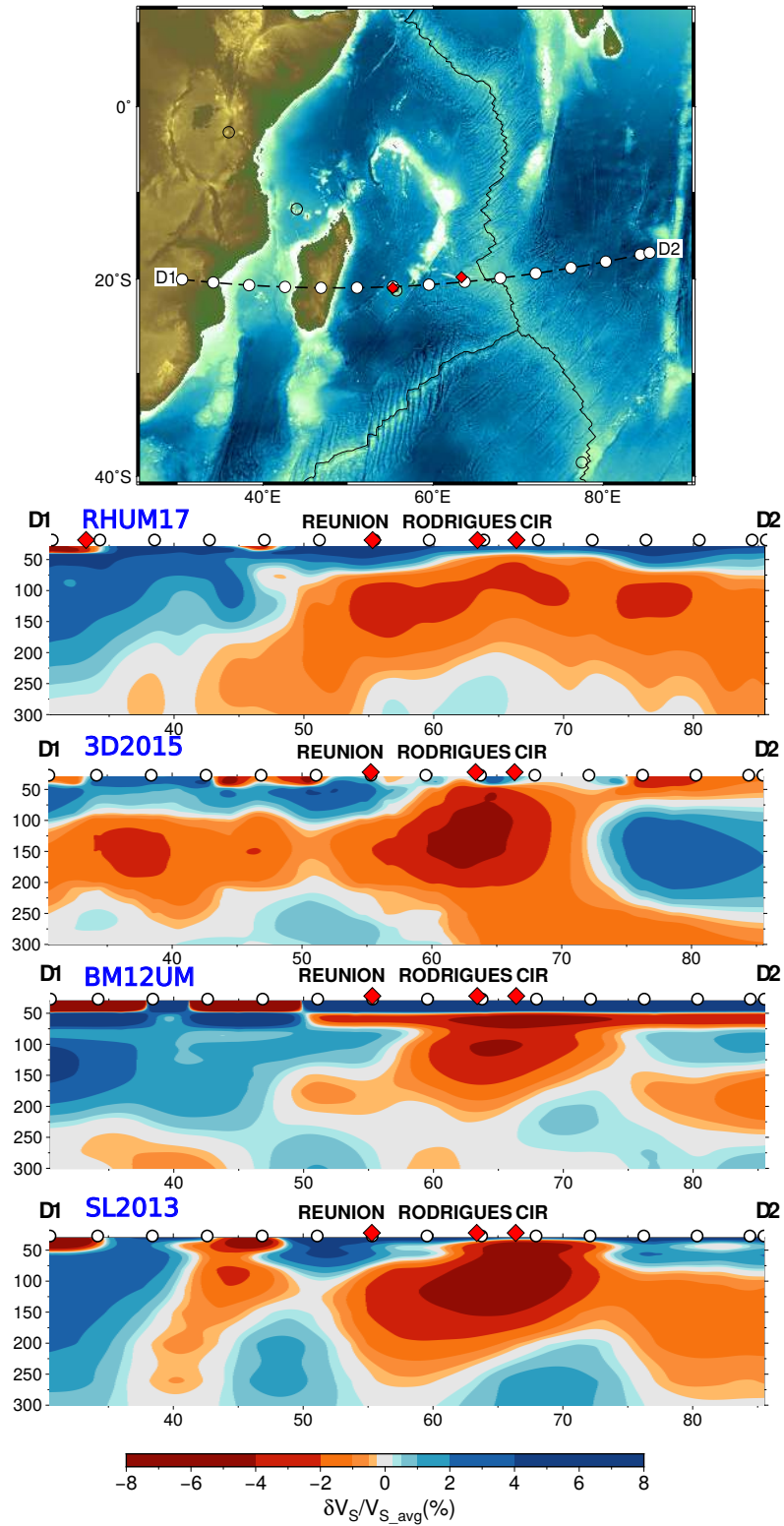
Figure S16. Vertical cross-section along line D1-D2 (top) through model RHUM17 and the three recent global models: BM12UM, SL2013sv, and 3D2015
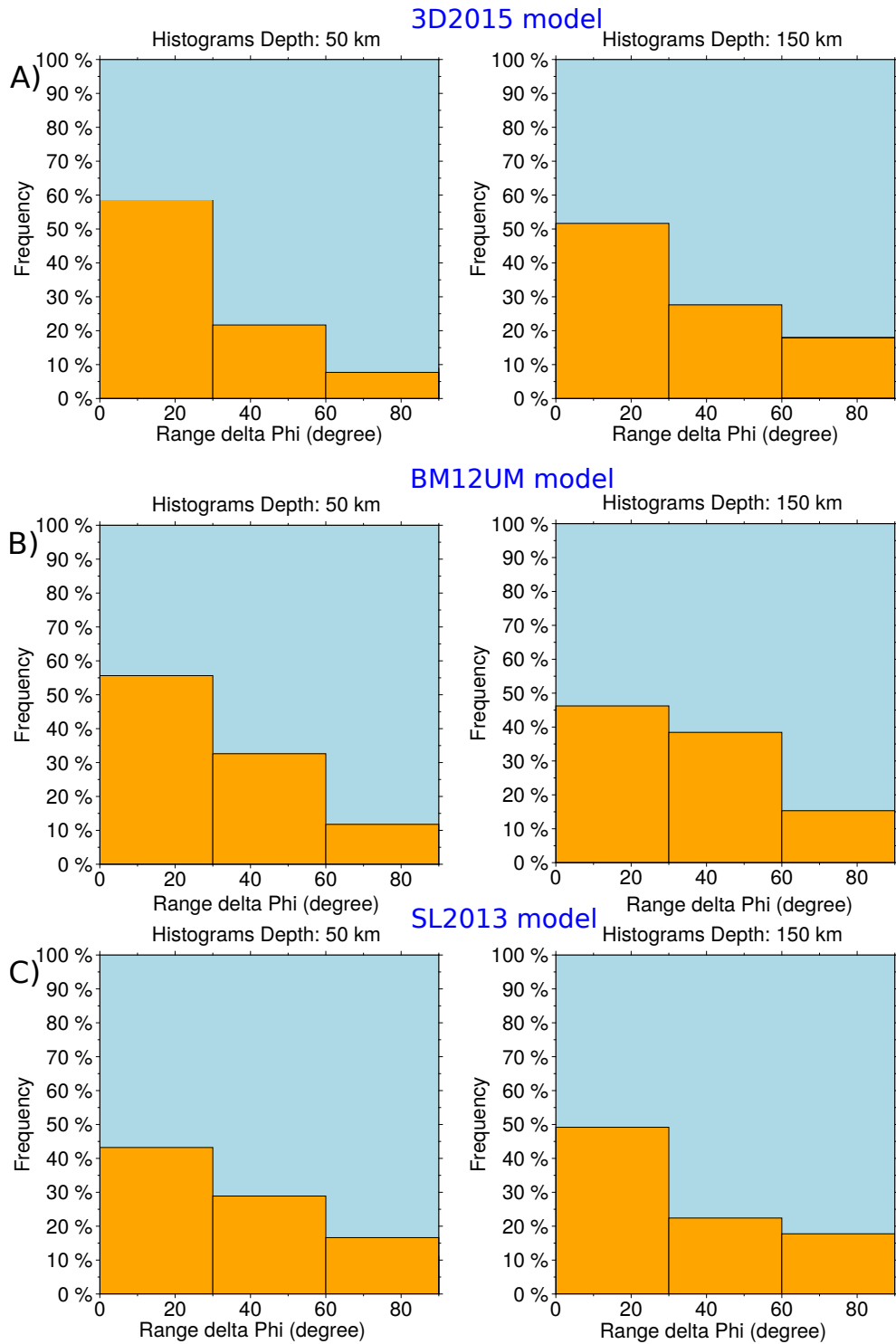
Figure S17. Histogram of the difference between the azimuthal fast direction in the present

model and models 3D2015, BM12UM, and SL2013 at 50 km (left) and 150 km (right) in depth.
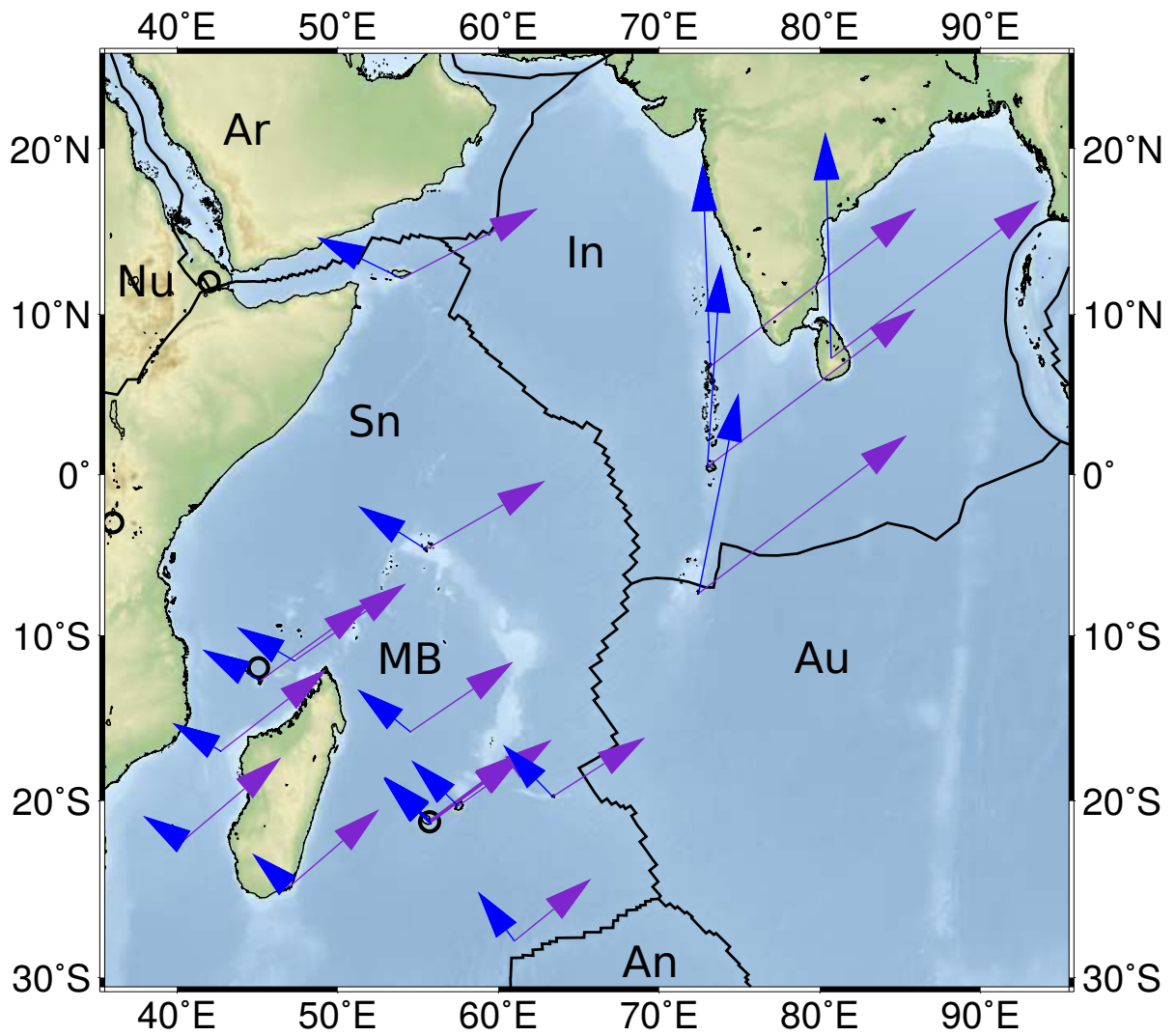
Figure S18.   Two absolute plate motion (APM) vectors at land station locations are shown, from the HS3-Nuvel1A model in blue, from the GSRM model in purple. The black circles indicate the hotspot location in the region. An, Antarctica plate; Ar, Arabian plate; Au, Australian plate; In, Indian plate; MB, Mascarene Basin; Nu, Nubian plate; Sn, Somali plate.
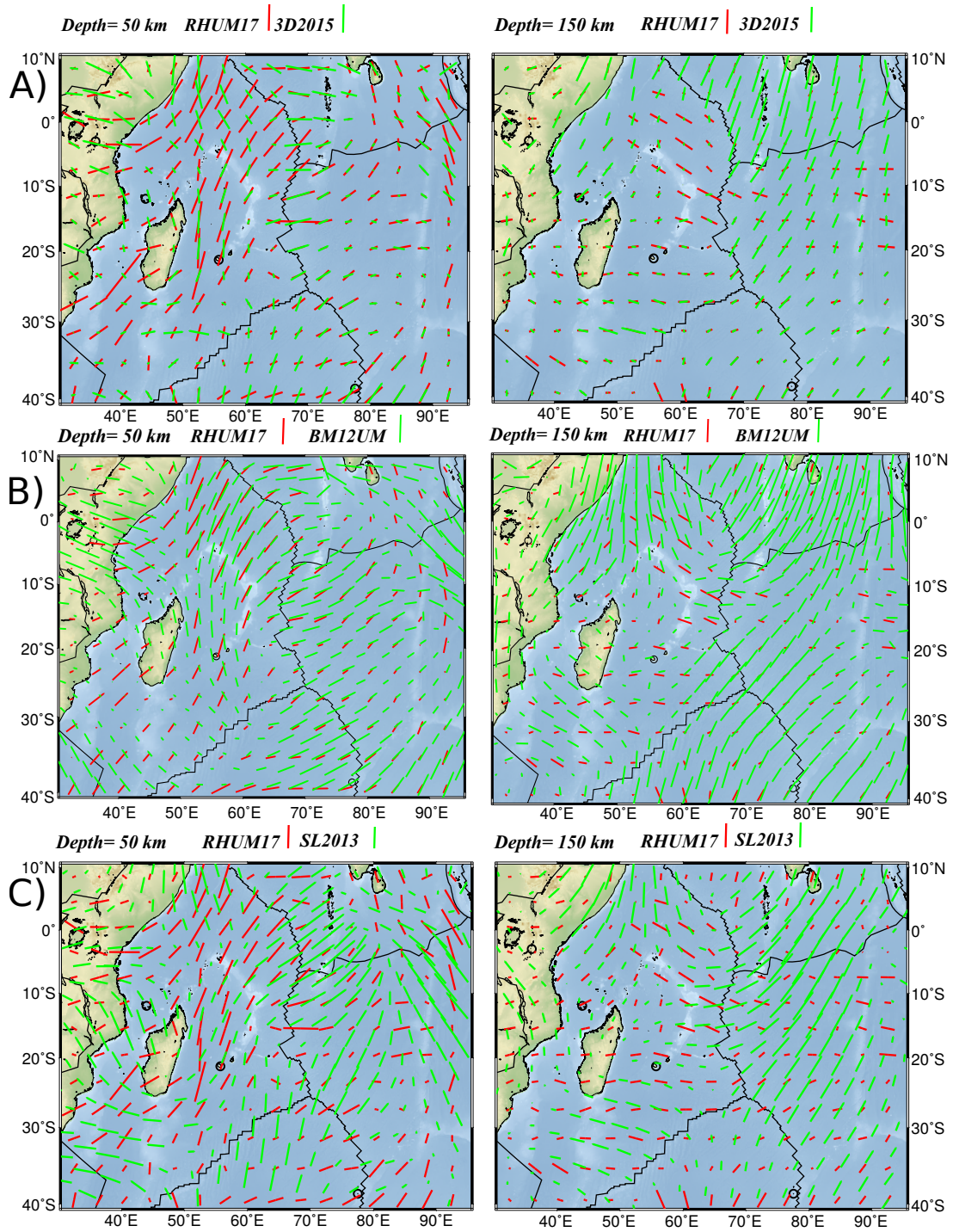
Figure S19. Comparison of azimuthal anisotropy directions between the present model (red line) and the three recent global models, 3D2015, BM12UM, and SL2013, at 50 and 150 km in depth (green line).

References

Bassin C., G. Laske, and G. Masters (2000), The current limits of resolution for surface wave tomography in North America, *OS Trans. AGU*, *81*(F897).

Burgos, G., J.-P. Montagner, E. Beucler, Y. Capdeville, A. Mocquet, and M. Drilleau (2014), Oceanic lithosphere-asthenosphere boundary from surface wave dispersion data, *Journal of Geophysical Research: Solid Earth*, *119*(2), 1079–1093.

Debayle, E., and M. Sambridge (2004), Inversion of massive surface wave data sets: Model construction and resolution assessment, *Journal of Geophysical Research*, *109*, doi: 10.1029/2003JB002652.

Debayle, E., F. Dubuffet, and S. Durand (2016), An automatically updated s-wave model of the upper mantle and the depth extent of azimuthal anisotropy, *Geophysical Research Letters*, *43*(2), 674–682.

Nolet G. (1990). Partitioned waveform inversion and two-dimensional structure under the network of autonomously recording seismographs, *Journal of Geophysical Research: Solid Earth*, *95*(B6), 8499–8512.

Schaeffer, A., and S. Lebedev (2013), Global shear speed structure of the upper mantle and transition zone, *Geophysical Journal International*.